Water Extract of Senecio scandens Buch.-Ham. Ameliorates Allergic Contact Dermatitis by Targeting MrgprB2 and Restoring Sustained Potassium Currents in Dorsal Root Ganglion Neurons

Shuo Jin
College of Pharmaceutical Sciences, Jishou University
Jingting Zhang
College of Pharmaceutical Sciences, Jishou University
Bing Li
Xiangxi Tujia and Miao Autonomous Prefecture Ethnic Traditional Chinese Medicine Hospital
Qingmei Cai
Guangdong Huidakang Pharmaceutical Co., Ltd.
Fan Ye
752045146@qq.com
College of Pharmaceutical Sciences, Jishou University
Gongxi Chen
College of Pharmaceutical Sciences, Jishou University

Research Article

Keywords: Senecio scandens Buch.-Ham., allergic contact dermatitis, MrgprB2, sustained potassium currents, metabolomics, gut microbiota

Posted Date: August 14th, 2026

DOI: https://doi.org/10.21203/rs.3.rs-10680607/v1

Additional Declarations: No competing interests reported.

Water Extract of *Senecio scandens* Buch.-Ham. Ameliorates Allergic Contact Dermatitis by Targeting MrgprB2 and Restoring Sustained Potassium Currents in Dorsal Root Ganglion Neurons

Shuo Jin[1,3], Jingting Zhang[1,3], Bing Li[2], Qingmei Cai[4], Fan Ye[1,3*], Gongxi Chen[1*]

[1]College of Pharmaceutical Sciences, Jishou University, Jishou 416000, China.

[2]Xiangxi Tujia and Miao Autonomous Prefecture Ethnic Traditional Chinese Medicine Hospital, Jishou 416000, China.

[3]Chemical and Pharmacological Laboratory of Medicinal Resources in Wuling Mountain Area, Jishou 416000, China.

[4]Guangdong Huidakang Pharmaceutical Co., Ltd., Foshan 528244, China.

[*]Correspondence address: Tel: +86-18874369722; E-mail: 752045146@qq.com (F. Y.) / E-mail: chengongxi2011@163.com (G.C.)

Abstract:

Background: Allergic contact dermatitis (ACD) is a common type IV hypersensitivity skin disorder characterized by recurrent inflammatory lesions and persistent pruritus. Although glucocorticoids are first-line treatments, their long-term use is limited by adverse effects. Mas-related G protein-coupled receptor B2 (MrgprB2) is a key regulator of allergic pruritus. Water extract of *S. scandens* (WSS) has anti-inflammatory and anti-allergic properties; however, its effects on neuronal excitability and its associations with the gut microbiota and host metabolism remain unclear.

Purpose: This study investigated the therapeutic mechanisms of WSS in ACD, focusing on MrgprB2-associated changes in dorsal root ganglion (DRG) excitability and potential contributions of the gut microbiota and serum metabolome.

Methods: Oxazolone-induced ACD models were established in C57BL/6J and MrgprB2$^{-/-}$ mice. Clinical scoring, 16S rRNA gene sequencing of the gut microbiota, untargeted serum metabolomics, whole-cell patch-clamp recordings, and enzyme-linked immunosorbent assays were used to assess treatment effects and potential mechanisms.

Results: WSS significantly reduced skin lesions and pruritus in C57BL/6J ACD mice, with effects comparable to those of hydrocortisone; these effects were not detected in MrgprB2$^{-/-}$ mice. In C57BL/6J mice, WSS altered gut microbial composition, partially restored the serum metabolic profile, and reduced cutaneous pro-inflammatory and pruritogenic mediators. Electrophysiological recordings showed that WSS reduced DRG neuronal hyperexcitability and restored sustained voltage-gated potassium currents. These changes were attenuated or absent in MrgprB2$^{-/-}$ mice, whereas sodium currents were not significantly affected.

Conclusion: WSS ameliorated ACD in C57BL/6J mice and was associated with restoration of sustained potassium currents in DRG neurons. The loss of efficacy in MrgprB2$^{-/-}$ mice suggests an essential role for MrgprB2, while the microbiome and metabolomic findings identify additional pathways for future mechanistic investigation.

Key Words: *Senecio scandens* Buch.-Ham.; allergic contact dermatitis; MrgprB2; sustained potassium currents; metabolomics; gut microbiota

1. Introduction

Allergic contact dermatitis (ACD) is a type IV hypersensitivity reaction to contact haptens [1]. Clinically, ACD presents with inflammatory skin lesions, including erythema, papules, and exudation, and is often accompanied by persistent pruritus. It frequently recurs and can substantially impair patients' quality of life. Glucocorticoids are currently first-line treatments. Although they can rapidly suppress inflammation, prolonged topical or systemic use may cause adverse effects, including skin atrophy, immunosuppression, and metabolic disturbances [2]. These limitations have prompted the search for safe, multitarget anti-inflammatory agents derived from natural medicines and investigation of their mechanisms of action.

Peripheral sensitization is a central pathological process underlying pruritus in ACD. Following cutaneous exposure to allergens, mast cells are activated and degranulate, releasing pruritogenic and pro-inflammatory mediators. These mediators can directly or indirectly sensitize primary sensory neurons in the dorsal root ganglia (DRG), thereby increasing neuronal excitability and transmitting sensory signals to the central nervous system [3,4]. Mas-related G protein-coupled receptor B2 (MrgprB2) is reported to be highly and selectively expressed in mast cells [5]. As an important mediator of mast-cell degranulation [6], MrgprB2 contributes to nonhistaminergic pruritus and allergic inflammation and may represent a therapeutic target for ACD [7].

Senecio scandens Buch.-Ham. ex D. Don (*S. scandens*) is a perennial herb in the genus Senecio, family Asteraceae. In traditional Chinese medicine, it is used to clear heat and detoxify and has been used in folk medicine to treat inflammatory skin

conditions, including sores, boils, swelling, pain, and eczema [8]. Existing literature has documented that the *S. scandens* possesses a broad range of biological activities, including anti-inflammatory, antibacterial, and anti-allergic effects. Our previous studies have demonstrated that water extract of *S. scandens* (WSS) exerts an ameliorative effect on ACD through regulation of the MrgprB2 pathway [9]. However, whether WSS alters sensory-neuron excitability through this pathway remains unknown.

Growing interest in the "gut-skin axis" has highlighted the potential regulatory roles of the gut microbiota and its metabolites in inflammatory skin diseases. Gut microbial dysbiosis may influence peripheral nerve excitability and cutaneous inflammatory responses by disrupting immune homeostasis and altering circulating metabolite profiles [10]. Evidence indicates that MrgprB2 not only mediates mast-cell degranulation and nonhistaminergic pruritus but can also respond to host antimicrobial peptides and microbiota-derived antibacterial metabolites. By inducing mast cells to release antimicrobial effector molecules, MrgprB2 may contribute to innate immune defense in the skin and intestinal mucosa and may link microbial homeostasis, antimicrobial immunity, and inflammatory responses [5].

Accordingly, we established oxazolone-induced ACD models in C57BL/6J and MrgprB2$^{-/-}$ mice. We integrated 16S rRNA gene sequencing of the gut microbiota, untargeted serum metabolomics, and whole-cell patch-clamp electrophysiology to investigate the effects of WSS on clinical phenotype, inflammatory mediators, microbial and host metabolism, and neuronal excitability. We also examined the

contribution of MrgprB2 to these effects. The findings provide a basis for further development of *S. scandens*-derived interventions and MrgprB2-targeted therapies for ACD.

2. Materials and Methods

2.1 Materials and Instruments

2.1.1 Experimental Animals

C57BL/6J mice, male, aged 6–8 weeks, weighing 19–22 g, specific pathogen-free (SPF) grade, were purchased from Tianqin Biotechnology Co., Ltd., Changsha, China. MrgprB2$^{-/-}$ mice, male, aged 6–8 weeks, weighing 19–22 g, SPF grade, were provided by Nanjing University of Chinese Medicine. The mice were fed with standard diet and maintained in a controlled environment at a constant temperature (23°C ± 2°C) and humidity (55% ± 15%), with a 12-h light/dark cycle. All mouse procedures were performed in accordance with the "Jishou University Guide for the Care and Use of Laboratory Animals" and followed the 3R principles. The animal experiments were approved by the Jishou University Biomedical Ethics Committee (No. JSDX-2025-0080). Only male mice were used in this study to eliminate potential confounding effects of the estrous cycle on inflammatory responses and pruritic behaviors in females.

2.1.2 Experimental Materials

S. scandens (Taizhou Hospital of Traditional Chinese Medicine, China); Hydrocortisone Aceponate Spray (Virbac S.A., France); DMEM/F-12 (Gibco, USA);

fetal bovine serum (Gibco, USA); penicillin-streptomycin (Gibco, USA); poly-D-lysine (Sigma, USA); laminin (Sigma, USA); nerve growth factor (NGF, Sigma, USA); D-Hank's solution (Gibco, USA); trypsin (Sigma, USA); collagenase (Sigma, USA); isoflurane (RWD Life Science Co., Ltd., China); cell strainer (Shanghai Jing'an Biotechnology Co., Ltd., China); cesium hydroxide, sodium chloride, magnesium chloride, potassium gluconate, calcium chloride, EGTA, HEPES, glucose, sucrose, potassium hydroxide, choline chloride, cadmium chloride, tetraethylammonium chloride, cesium fluoride (all purchased from Sinopharm Chemical Reagent Co., Ltd., China); Interleukin-17A (IL-17A), Interleukin-1β (IL-1β), Tumor Necrosis Factor α (TNF-α), Interleukin-4 (IL-4), Interleukin-13 (IL-13), histamine (HIS), 5-hydroxytryptamine (5-HT), C-X-C motif chemokine ligand 10 (CXCL10), and Trypsin Beta 2 (TPSβ2) kits (all purchased from Ruixin Biotechnology Co., Ltd., China).

2.1.3 Experimental Instruments

Anesthesia machine (Shenzhen RWD Life Science Co., Ltd., China); hair clipper (Flyco, China); syringe (Changzhou Yuekang Medical Equipment Co., Ltd., China); video camera (Shanghai Suoguang Electronics Co., Ltd., China); video recording box (self-made); ExionLC liquid chromatography system, TripleTOF 6600 mass spectrometer (AB Sciex, USA); Vanquish ultra-high performance liquid chromatograph (Thermo Scientific, USA).

Electrophysiological experimental operating system: vibration isolation table

(TMC, USA); Faraday cage (Dongle, China); perfusion and drug delivery system (Warner, USA); constant-flow peristaltic pump (Baoding Lange Co., Ltd., UK); inverted fluorescence DIC phase-contrast microscope (Zeiss, Germany); CCD camera (Olympus, Japan); micropipette puller (Sutter, USA); 700B amplifier (AXON, USA); 1440A digitizer (AXON, USA); micromanipulator (Scientifica, UK); microscope moving platform (Siskiyou, USA); osmometer (Osmomat 030, Germany); data acquisition software (Clampex 10.3).

2.2 Preparation and Component Determination of WSS

Briefly, 10 g of *S. scandens* decoction pieces was mixed with ultrapure water at a solid-liquid ratio of 1:10 (g/mL). Heat reflux extraction was performed 3 times for 2 hours each. The extracts were combined and filtered under suction to remove the residue. The filtrate was concentrated under reduced pressure at 50 °C with a rotation speed of 60 r/min to obtain WSS. After thorough vortex mixing, WSS was centrifuged at 5500 g for 10 min, and the supernatant was collected for subsequent injection analysis.

UHPLC-MS/MS conditions:

(1) Chromatographic conditions: Separation was performed on an Ultimate XB-C18 column (4.6 mm × 150 mm, 3 μm) with a column temperature of 40 °C. The injection volume was 10 μL, and the flow rate was 0.6 mL/min. The mobile phase consisted of phase A (deionized water containing 0.1% formic acid) and phase B

(acetonitrile containing 0.1% formic acid) with gradient elution. The detailed gradient elution parameters are shown in Table 1.

Table 1 Chromatographic elution conditions

Time	Flow rate (ml/min)	%A	%B
3	0.6	95	5
24	0.6	5	95
32	0.6	5	95
32.01	0.6	95	5
40	0.6	Stop	

(2) Mass spectrometric conditions: Mass spectrometric data were acquired using a TripleTOF 6600 mass spectrometer with multiple reaction monitoring scan mode in both positive and negative ion modes. The curtain gas pressure was set to 40.00 psi, nebulizer gas (GS1) to 60.00 psi, auxiliary gas (GS2) to 60.00 psi, ion spray voltage to 4.5 kV, and nebulizer gas temperature to 550.00 °C. Using SCIEX OS software, compound information was extracted from total ion current chromatograms of samples in positive and negative ion modes based on existing literature. Compounds were identified by aligning tandem mass spectra with relevant literature reports and the PubChem database.

2.3 Therapeutic Effect of WSS on ACD Mice

After adaptive feeding, C57BL/6J and MrgprB2$^{-/-}$ mice were randomly divided into 4 groups according to body weight: control group, model group, WSS group, and hydrocortisone (HC) group. The hair on the nape and abdomen of mice (1.5 cm × 2 cm area) was shaved, and remaining villi were further removed with depilatory cream. After 3 days of adaptation, 3% oxazolone was applied to the abdomen for sensitization for 3 consecutive days. A 30-minute video recording was performed after the last sensitization as baseline. On the next day, 1% oxazolone was applied to the nape. Mice in the WSS group received intragastric administration of 3.9 g/kg/d WSS 1 h before oxazolone challenge [9]. Mice in the HC group were topically sprayed with hydrocortisone aceponate 1 h before oxazolone model induction, at a daily dose of 1.52 μg per cm² of skin area (calculated as hydrocortisone aceponate). Behavioral video recording was performed for 30 min immediately after challenge, and scoring was conducted for 3 consecutive days. Following behavioral testing, skin lesions on the nape of mice were photographed and evaluated across three dimensions: erythema and edema, skin wrinkling, and excoriation, with each parameter scored on a 0–3 scale. After modeling, serum samples were collected, and skin tissues from the back lesion area were excised with surgical scissors and stored at -80 ℃. Mice were euthanized by an overdose of isoflurane.

2.4 Gut Microbiota Analysis

Fresh fecal samples were collected aseptically, immediately frozen, and stored at -80 ℃. Total bacterial DNA was extracted and purified for 16S rRNA sequencing.

The V3-V4 hypervariable region of the 16S rRNA gene was amplified with primers 338F and 806R and sequenced by Majorbio Bio-Pharm Technology Co., Ltd. (Shanghai, China). All bioinformatics analyses were performed on the Majorbio Cloud Platform (https://cloud.majorbio.com/page/tools/).

2.5 Untargeted Metabolomics

2.5.1 Metabolite Extraction

Serum samples were thawed slowly at 4 °C. An appropriate volume of sample was mixed with pre-cooled methanol/acetonitrile/water (2:2:1, v/v/v), followed by vortex mixing and low-temperature ultrasonication for 30 min. The mixture was incubated at -20 °C for 10 min and centrifuged at 14000 g for 20 min at 4 °C. The supernatant was collected and dried under vacuum. For mass spectrometry analysis, the dried extract was reconstituted with 100 μL of acetonitrile/water solution (acetonitrile:water = 1:1, v/v), vortexed, and centrifuged at 14000 g for 15 min at 4 °C. The supernatant was collected for injection analysis.

2.5.2 UPLC-Q-TOF-MS Conditions

(1) Chromatographic conditions: Samples were separated on an Agilent 1290 Infinity LC ultra-high performance liquid chromatography (UHPLC) system equipped with a HILIC column. The column temperature was set at 25 °C, the flow rate was 0.5 mL/min, and the injection volume was 2 μL. The mobile phase consisted of phase A (water with 25 mM ammonium acetate and 25 mM ammonia) and phase B

(acetonitrile). The gradient elution program was as follows: 0–0.5 min, 95% B; 0.5–5 min, B decreased linearly from 95% to 65%; 5–5.5 min, B decreased linearly from 65% to 40%; 5.5–6 min, B increased linearly from 40% to 95%; 6–8 min, B maintained at 95%. During the entire analysis, samples were placed in the autosampler at 4 °C and analyzed in random order. Quality control (QC) samples were inserted into the sample queue to monitor and evaluate system stability.

(2) Mass spectrometric conditions: A Triple TOF 6600 mass spectrometer (AB SCIEX) was used to acquire primary and secondary mass spectra of samples. After separation by the Agilent 1290 Infinity LC UHPLC system, samples were analyzed by mass spectrometry in both electrospray ionization (ESI) positive and negative ion modes.

The ESI source parameters were set as follows: nebulizer gas 1 (Gas1): 60, auxiliary gas 2 (Gas2): 60, curtain gas: 30 psi, ion source temperature: 600 °C, ion spray voltage floating: ±5500 V for positive and negative modes. The mass-to-charge ratio (m/z) range for primary MS detection was 60–1000 Da, and that for secondary product ions was 25–1000 Da. The accumulation time for primary MS scans was 0.20 s per spectrum, and 0.05 s per spectrum for secondary MS scans. Secondary mass spectra were acquired in information-dependent acquisition mode with peak intensity screening. The declustering potential was ±60 V for positive and negative modes, and the collision energy was 35 ± 15 eV. IDA settings were as follows: isotope ions within 4 Da were dynamically excluded, and 10 fragment spectra were acquired per scan.

234

235 2.5.3 Data Processing

236 Raw data were converted via ProteoWizard and processed by XCMS software
237 for peak alignment, retention time correction, and peak area extraction. For the data
238 extracted by XCMS, metabolite structure identification was first performed using an
239 in-house standard database (Shanghai Applied Protein Technology) [11,12].
240 Metabolite structures in biological samples were identified by matching retention time,
241 molecular mass (mass error < 10 ppm), tandem fragmentation spectra, and collision
242 energy with metabolites in the local database, and the identification results were
243 strictly manually reviewed and confirmed. All identifications were above Level 2
244 confidence. After data preprocessing (null value filtering, null value imputation, data
245 filtering) and experimental data quality evaluation, subsequent analyses were
246 performed, including principal component analysis (PCA) and orthogonal partial least
247 squares-discriminant analysis (OPLS-DA).

248 Variable importance in the projection (VIP) values were obtained from the
249 OPLS-DA model. Significantly differential metabolites were screened with the
250 criteria of OPLS-DA VIP > 1.0, Student's *t*-test *P*-value < 0.05, and fold change > 1.0
251 or < 1.0 [13]. Kyoto Encyclopedia of Genes and Genomes (KEGG) database
252 (https://www.kegg.jp/) was used for pathway enrichment analysis of differential
253 metabolites. The differential abundance score plot of enriched metabolic pathways
254 was generated based on the differential abundance score. Key biomarkers of *S.*
255 *scandens* in ACD treatment were screened according to differential metabolites

involved in these critical metabolic pathways [14,15].

2.6 ELISA Assay

Skin lesion tissues from each group were homogenized and extracted, followed by protein quantification. The levels of IL-17A, IL-1β, TNF-α, IL-4, IL-13, HIS, 5-HT, CXCL10, and TPSβ2 in the extracts were detected according to the ELISA kit instructions.

2.7 Evaluation of the Effect of WSS on MrgprB2-Mediated DRG Excitability

2.7.1 Isolation and Culture of DRG Neurons

On day 3 after modeling, mice were sacrificed under deep anesthesia, and dorsal root ganglia from cervical segments C1–C7 were rapidly dissected. Tissues were digested with trypsin-collagenase mixture at 37 °C for 20 min, then gently triturated to prepare a single-cell suspension. After filtration, the suspension was centrifuged at 1200 r/min for 5 min. The cell pellet was resuspended in DMEM/F-12 medium containing 10% fetal bovine serum, and seeded onto coverslips pre-coated with poly-D-lysine and laminin. After 40 min of incubation at 37 °C for cell attachment, nerve growth factor was added at a final concentration of 10 ng/mL. Electrophysiological recordings were performed after 4 h of culture.

2.7.2 Detection of Excitability in DRG neurons

Whole-cell patch-clamp recordings were performed in current-clamp mode. The extracellular solution and pipette internal solution were prepared according to standard electrophysiological protocols (pH 7.3–7.4, osmolarity 310 mOsm). A 500-ms ramp current stimulus ranging from 0 to 1 nA was applied to record the number of evoked action potentials. Subsequently, 200-ms step current stimuli ranging from 0 to 500 pA with 10-pA increments were delivered to determine the rheobase, defined as the minimum current threshold for action potential generation. For MrgprB2$^{-/-}$ mice with lower excitability, rheobase was measured using step current stimuli ranging from 0 to 1.2 nA with 100-pA increments. The number of action potentials, rheobase, and resting membrane potential were statistically analyzed across groups.

2.7.3 Detection of Sodium Currents in DRG neurons

Recordings were conducted in voltage-clamp mode. The extracellular solution was formulated with choline chloride replacing most sodium chloride, supplemented with tetraethylammonium chloride and cadmium chloride to block potassium and calcium currents. The pipette internal solution was mainly composed of cesium fluoride (pH 7.3–7.4, osmolarity 310 mOsm). With a holding potential of −100 mV, 30-ms depolarizing step pulses from −100 mV to +50 mV in 10-mV increments were applied to record total voltage-gated sodium currents. After 3 min of perfusion with 300 nmol/L tetrodotoxin (TTX), the holding potential was adjusted to −50 mV, and the same stimulation protocol was delivered to record TTX-resistant (TTX-R) sodium

currents. TTX-sensitive (TTX-S) sodium currents were calculated as the difference between total sodium currents and TTX-R sodium currents. The peak current amplitude at each test potential was collected.

2.7.4 Detection of Potassium Currents in DRG neurons

Recordings were performed in voltage-clamp mode. Cadmium chloride was added to the extracellular solution to block calcium currents, and the pipette internal solution was mainly composed of potassium gluconate (pH 7.3–7.4, osmolarity 310 mOsm). With a holding potential of −100 mV, 500-ms depolarizing step pulses from −60 mV to +50 mV in 10-mV increments were applied to record total voltage-gated potassium currents. The holding potential was then adjusted to −40 mV, and the same protocol was used to record sustained potassium currents. Transient potassium currents were calculated as the difference between total and sustained potassium currents. The current amplitude at each test potential was collected.

2.8 Statistical Analysis

GraphPad Prism 8.0 was used for statistical analysis. Unpaired t-test was applied for comparisons between two groups, and one-way analysis of variance (One-Way ANOVA) was used for comparisons among multiple groups, followed by Dunnett's multiple comparisons test for post-hoc pairwise comparisons. A p-value < 0.05 was considered statistically significant. All error bars in the figures represent the standard error of the mean (SEM).

3. Results

3.1 Component Identification of WSS

Chemical profiling of WSS yielded 41 compound signals. Comparison of tandem mass spectra with published data and the PubChem database enabled putative identification of 22 compounds (Table 2). Total ion chromatograms (TICs) acquired in positive- and negative-ion modes are shown in Figure 1.

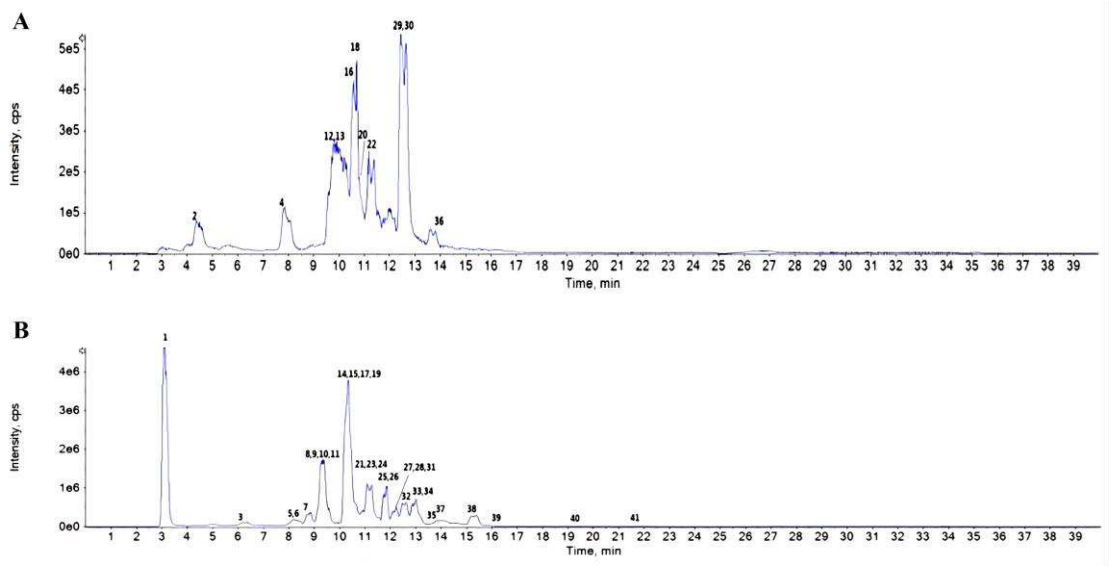

Figure 1. Total ion chromatograms of WSS acquired in positive- and negative-ion modes

(A) TIC of WSS in positive-ion mode; (B) TIC of WSS in negative-ion mode.

Table 2. Chemical components identified in WSS

No.	t_R/min	Molecular formula	Molecular weight	Ion mode	MS/（m/z）	Name
1	3.116	$C_7H_{12}O_6$	192.06	-	191.0560	D-quinic acid

3	6.246	$C_7H_6O_5$	170.12	-	169.0156	gallic acid
4	7.767	$C_9H_{11}NO_2$	165.08	+	166.0854	L-phenylalanine
6	8.425	$C_7H_6O_4$	154.12	-	153.0202	protocatechuic acid
8	9.165	$C_7H_6O_4$	154.12	-	153.0203	2,3-Dihydroxybenzoic acid
10	9.400	$C_{16}H_{18}O_9$	354.31	-	353.0889	cryptochlorogenic acid
14	10.322	$C_{16}H_{18}O_9$	354.31	-	353.0891	chlorogenic acid
16	10.524	$C_{21}H_{20}O_9$	416.38	+	417.1168	puerarin
20	10.977	$C_{18}H_{25}NO_5$	335.17	+	336.1788	senecionine
21	11.082	$C_9H_8O_4$	350.39	-	179.0364	(±)-caffeic acid
23	11.228	$C_9H_8O_4$	350.39	-	179.0363	(±)-caffeic acid
24	11.264	$C_7H_6O_4$	154.12	-	153.0201	2,5-dihydroxybenzoic acid
26	11.772	$C_{27}H_{30}O_{16}$	610.52	-	609.1483	rutin
27	12.153	$C_{21}H_{20}O_{12}$	464.38	-	463.0886	hyperoside
31	12.481	$C_{25}H_{24}O_{12}$	516.45	-	515.1200	isochlorogenic acid C
32	12.627	$C_9H_8O_3$	164.05	-	163.0414	3-Hydroxycinnamic acid
33	12.901	$C_{21}H_{20}O_{11}$	448.38	-	447.0939	quercitrin
34	13.120	$C_{10}H_{10}O_4$	194.18	-	193.0513	ferulic acid
36	13.805	$C_{15}H_{10}O_6$	286.24	+	287.0532	kaempferol
37	13.941	$C_7H_6O_4$	154.12	-	153.0200	2,6-Dihydroxybenzoic acid

38	15.366	$C_7H_6O_3$	138.03	-	137.0252	2-hydroxybenzoic acid
40	19.425	$C_{16}H_{12}O_5$	284.26	-	283.0616	acacetin
41	21.672	$C_{15}H_{10}O_5$	270.24	-	269.0454	emodin

3.2 MrgprB2 Contributes to the Therapeutic Effects of S. scandens in ACD

An ACD model was established in C57BL/6J mice. As shown in Figure 2A,B, the skin lesion score was significantly higher in the model group than in the control group ($p < 0.001$), supporting successful model induction. Skin lesion scores were significantly lower in the WSS and HC groups than in the model group ($p < 0.001$). Analysis of scratching behavior (Supplementary Figure 1A) similarly showed that WSS significantly reduced ACD-associated pruritus relative to the model group ($p < 0.05$).

The ACD model was also established in MrgprB2$^{-/-}$ mice. As shown in Figure 2C,D, the skin lesion score was significantly higher in the model group than in the control group ($p < 0.001$), supporting successful model induction. Relative to the model group, hydrocortisone significantly reduced the skin lesion score ($p < 0.001$), whereas WSS did not. Analysis of scratching behavior (Supplementary Figure 1B) showed that hydrocortisone significantly reduced ACD-associated pruritus ($p < 0.001$), whereas WSS produced no significant change. Thus, the effects of WSS observed in C57BL/6J mice were not detected in MrgprB2$^{-/-}$ mice, consistent with a role for MrgprB2 in the response to WSS.

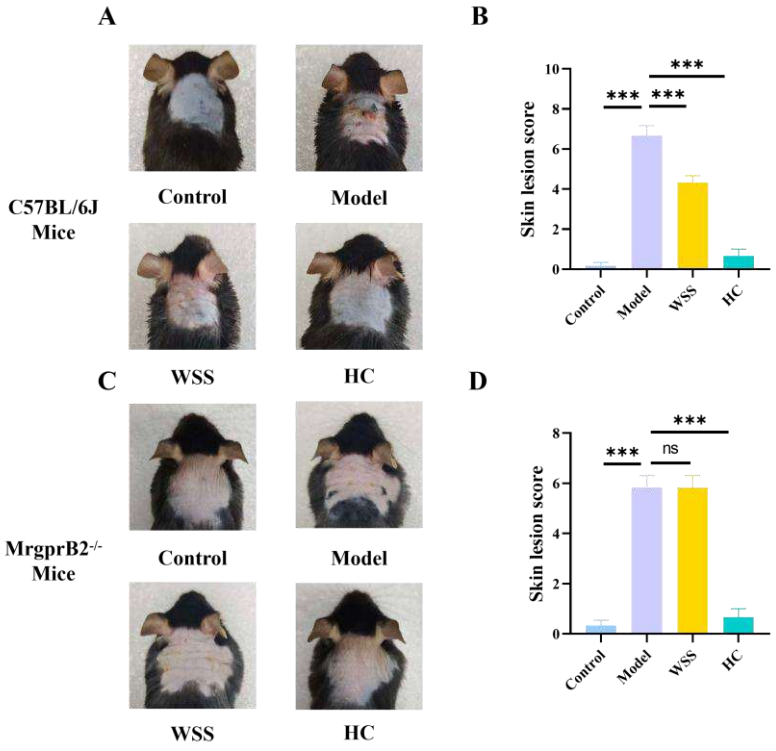

Figure 2. Effects of WSS on ACD skin lesions in C57BL/6J and MrgprB2$^{-/-}$ mice (A) Representative macroscopic appearance of ACD skin lesions in C57BL/6J mice; (B) skin-lesion severity scores across C57BL/6J groups (n = 6); (C) representative macroscopic appearance of ACD skin lesions in MrgprB2$^{-/-}$ mice; (D) skin-lesion severity scores across MrgprB2$^{-/-}$ groups (n = 6).

3.3 WSS Alters Gut Microbial Structure in an MrgprB2-Associated Manner

We assessed gut microbial richness and diversity in the two mouse strains using the ACE and Shannon indices and the Kruskal-Wallis rank-sum test. WSS did not significantly alter either index (Figure 3A, B). Principal coordinate analysis (PCoA) was used to examine differences in overall gut microbial structure (Figure 3C). Except for the weak within-group clustering of MrgprB2$^{-/-}$ WSS samples, samples in the other groups clustered relatively well. In C57BL/6J mice, the WSS and model groups were clearly separated. Hierarchical clustering produced a similar pattern

366 (Figure 3D), with greater separation between the WSS and model groups in C57BL/6J
367 mice than in MrgprB2$^{-/-}$ mice.

368 We next examined gut microbial composition at the genus level.
369 Community-composition bar plots (Figure 3E) and Kruskal-Wallis rank-sum tests
370 (Figure 3F) indicated that WSS primarily altered the relative abundance of
371 *Ligilactobacillus* in C57BL/6J mice. The relative abundance of *Ligilactobacillus* was
372 lower in ACD mice than in controls, and WSS treatment reversed this difference.
373 WSS also increased the relative abundance of *Odoribacte*r in ACD mice on the
374 C57BL/6J background.

375 PICRUSt2 was subsequently used to predict gene-family abundance in each
376 sample. Predicted gene families were mapped to the KEGG database to infer
377 functional profiles (Figure 4). In C57BL/6J mice, the predicted abundances of
378 pathways related to glycine, serine, and threonine metabolism; alanine, aspartate, and
379 glutamate metabolism; cysteine and methionine metabolism; amino acid biosynthesis;
380 pyruvate metabolism; two-component systems; quorum sensing; and carbon
381 metabolism were significantly higher in the WSS group than in the model group.

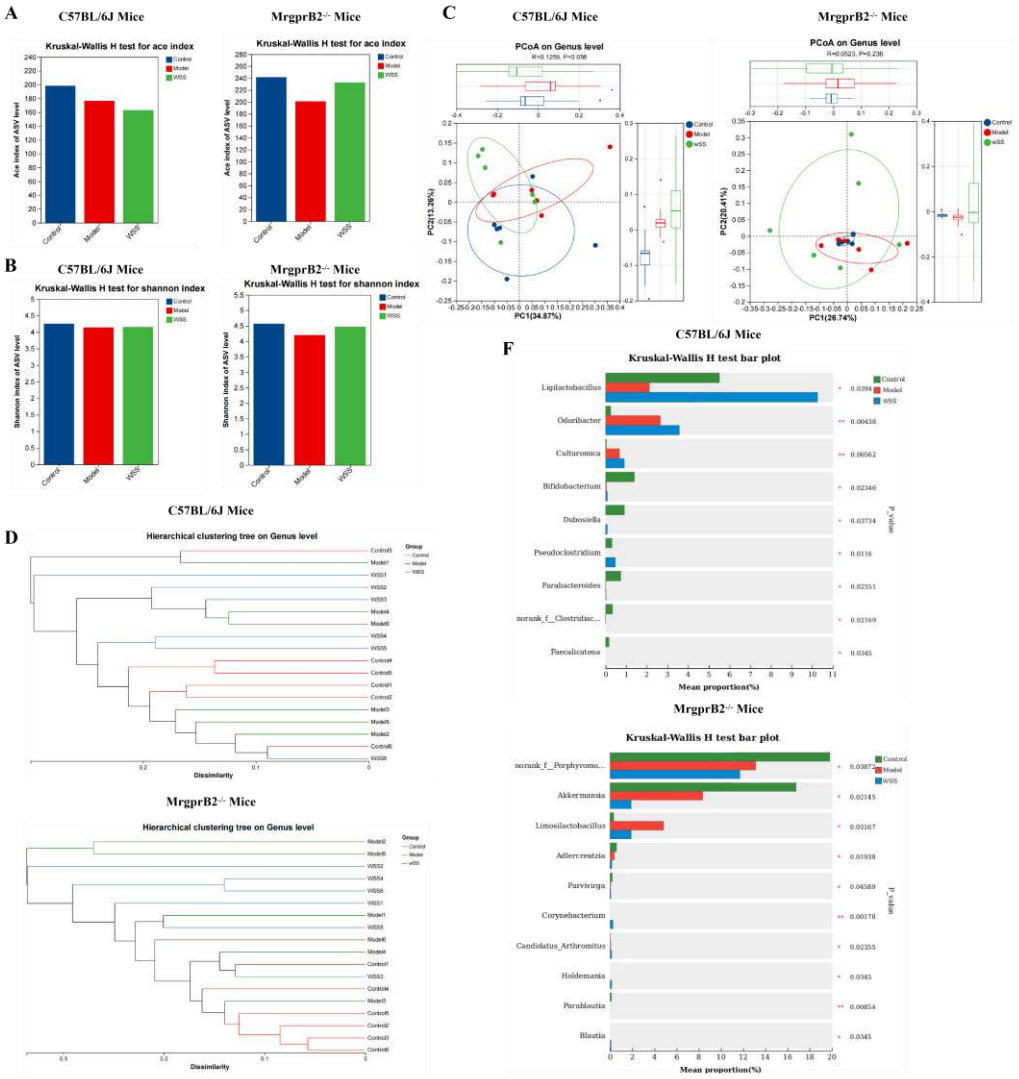
A
C57BL/6J Mice
MrgprB2-/- Mice
Kruskal-Wallis H test for ace index
B
Kruskal-Wallis H test for shannon index
C
PCoA on Genus level
D
Hierarchical clustering tree on Genus level
E
Community barplot analysis
F
Kruskal-Wallis H test bar plot
Mean proportion(%)
Control
Model
WSS

Figure 3. Effects of WSS on the gut microbiota of mice with different genotypes

(A) ACE index of alpha diversity; (B) Shannon index of alpha diversity; (C) principal coordinate analysis (PCoA); (D) hierarchical clustering dendrogram; (E) microbial community-composition bar plot; (F) multiple-taxon differential-abundance analysis. n = 6. $^{*}p < 0.05$; $^{**}p < 0.01$.

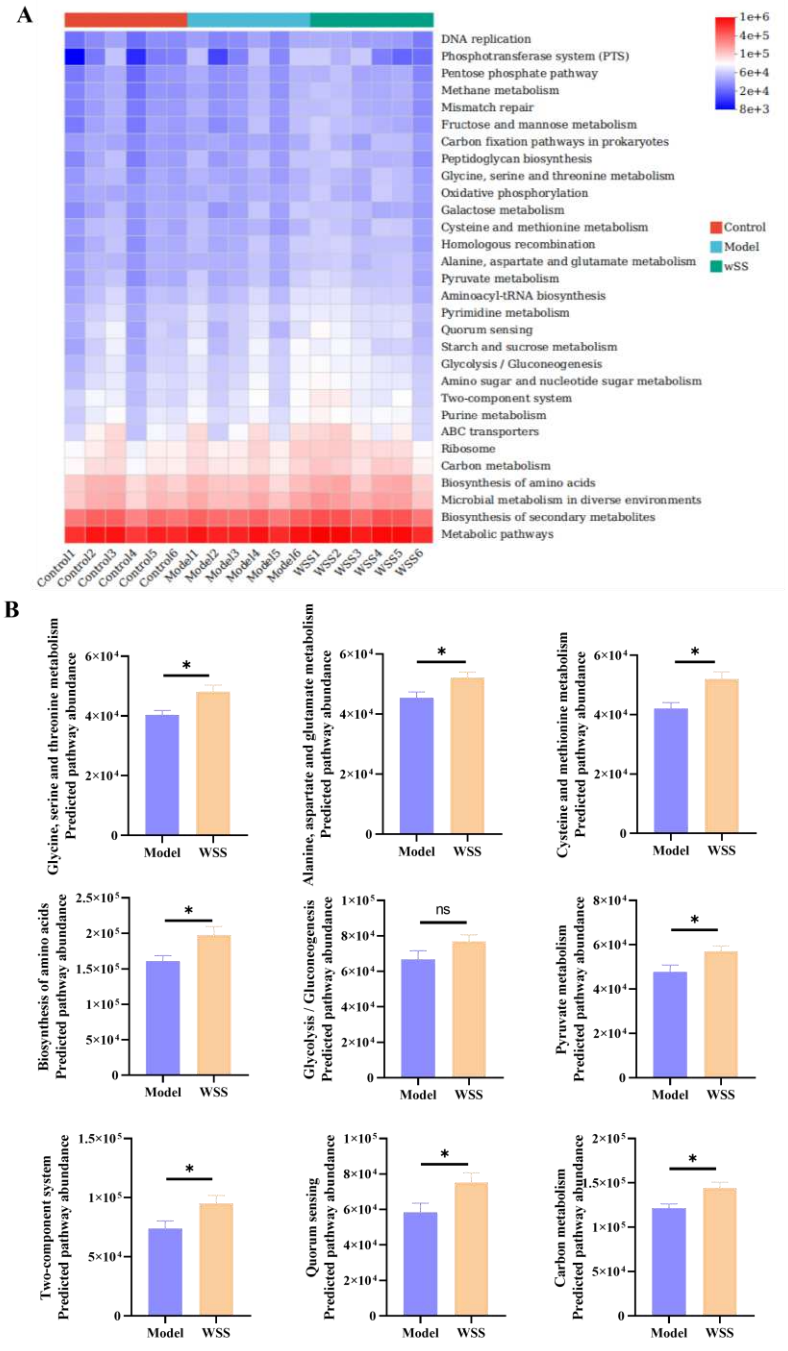

Figure 4. PICRUSt2-based functional prediction of the gut microbiota in C57BL/6J

mice

(A) Heatmap of predicted KEGG functional profiles; (B) comparison of predicted KEGG functional abundances. n = 6 per group. Data are presented as the mean ± SEM. $^{*}p < 0.05$; ns, not significant.

3.4 WSS Alters Serum Metabolism in an MrgprB2-Associated Manner

The tight clustering of QC samples in both positive- and negative-ion modes in the PCA and OPLS-DA score plots indicated good analytical reproducibility (Figure 5A,B). For both mouse strains, the WSS and model groups were separated. In C57BL/6J mice, the negative-ion metabolite profile of the WSS group was closer to that of the control group, whereas in MrgprB2$^{-/-}$ mice, the positive-ion profile was closer to that of the control group. These findings suggest that the metabolic responses to WSS differed between genotypes.

Differential metabolites were defined using VIP > 1.0 and $p < 0.05$. Relative to the model group, the WSS group had 19 upregulated and 39 downregulated differential metabolites in C57BL/6J mice and 28 upregulated and 23 downregulated metabolites in MrgprB2$^{-/-}$ mice (Figure 5C). The identified differential metabolites were visualized using clustered heatmaps (Figure 6).

KEGG pathway-enrichment analysis was then performed to identify pathways associated with the differential metabolites and explore potential mechanisms through which WSS ameliorates ACD. In C57BL/6J mice, differential metabolites between the WSS and model groups were mainly enriched in mineral absorption, ABC

transporters, and FcγR-mediated phagocytosis (Figure 7). In MrgprB2$^{-/-}$ mice, the main enriched pathways were nucleotide metabolism, folate biosynthesis, and pyrimidine metabolism.

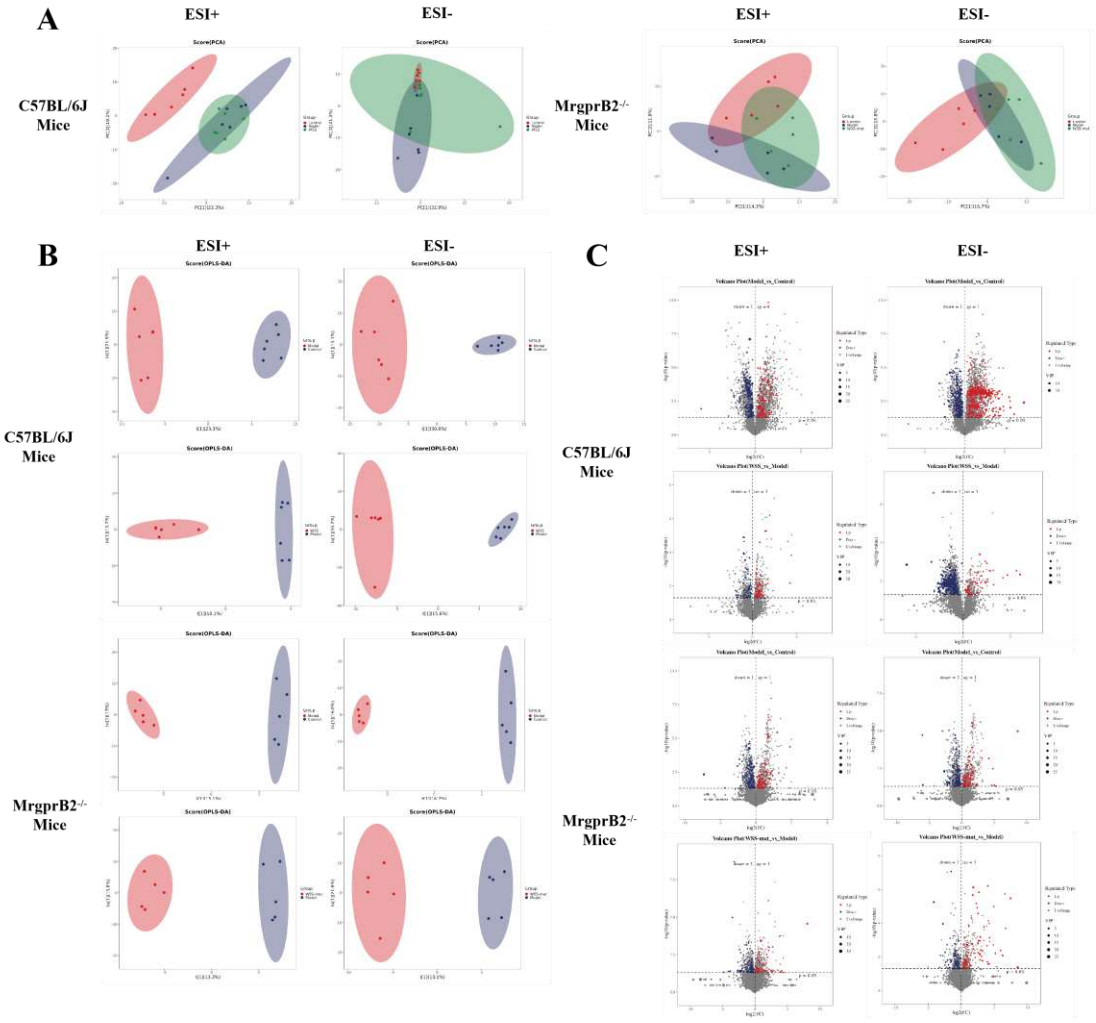

Figure 5. Effects of WSS on serum metabolic profiles

(A) PCA score plot; (B) OPLS-DA score plot; (C) volcano plot of differential metabolites with VIP scores. C57BL/6J mice, n = 6 per group; MrgprB2$^{-/-}$ mice, n = 5 per group.

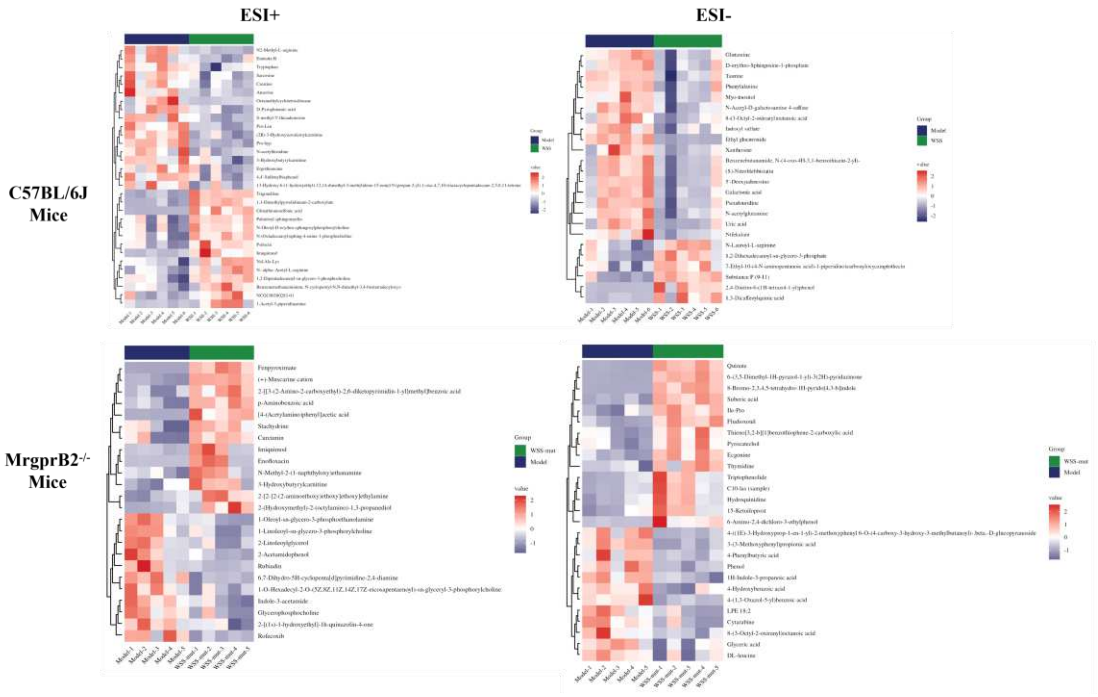

Figure 6. Clustered heatmap of differential metabolites (WSS vs. model)

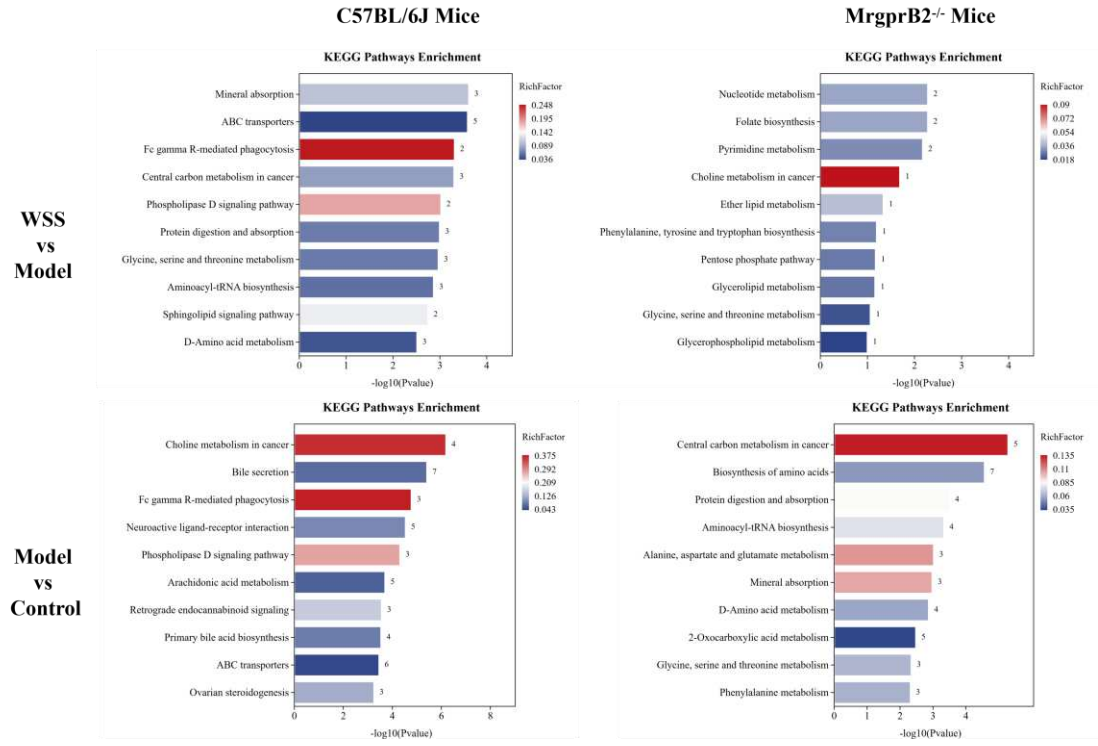

Figure 7. Effects of WSS on enriched serum metabolic pathways

3.5 WSS Alters Cutaneous Inflammatory and Pruritogenic Mediators in an MrgprB2-Associated Manner

In C57BL/6J mice, WSS significantly altered the cutaneous levels of TNF-α (Figure 8A; $p < 0.05$), 5-HT ($p < 0.001$), IL-4 ($p < 0.001$), and CXCL10($p < 0.05$). We then measured the same mediators in MrgprB2$^{-/-}$ mice. WSS significantly altered 5-HT and IL-4 levels (Figure 8B; $p < 0.05$), although the changes were smaller than those observed in C57BL/6J mice; TNF-α and CXCL10 levels did not change significantly.

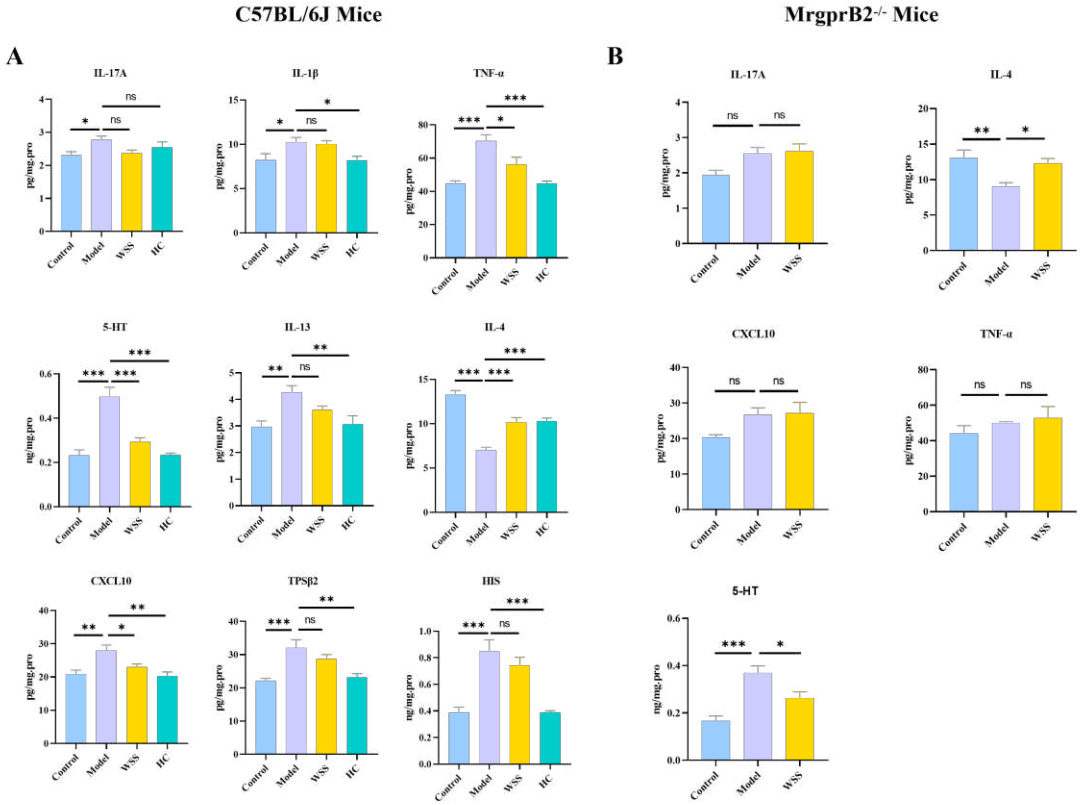

Figure 8. Effects of WSS on cutaneous inflammatory and pruritogenic mediators

(A) Effects of WSS on cutaneous mediators in C57BL/6J mice (n = 6); (B) effects of WSS on cutaneous mediators in MrgprB2$^{-/-}$ mice (n = 5). Data are presented as the mean ± SEM. $^{*}p < 0.05$; $^{**}p < 0.01$; $^{***}p < 0.001$; ns, not significant.

3.6 WSS Modulates DRG Neuronal Excitability in an MrgprB2-Associated

Manner

Pathways predicted from the gut microbiota—including glycine, serine, and threonine metabolism; alanine, aspartate, and glutamate metabolism; and cysteine and methionine metabolism—generate products such as amino acids, one-carbon units, short-chain fatty acids (SCFAs), and pyruvate that may influence electrical signaling in DRG neurons. Serum metabolomic pathways, including mineral absorption, ABC transporters, and FcγR-mediated phagocytosis, are likewise associated with ion homeostasis, membrane potential, the cellular microenvironment, and neuronal signaling. In addition, the ELISA results showed changes in TNF-α and 5-HT, mediators associated with mast-cell degranulation and sensory-neuron activation. We therefore investigated whether the effects of WSS on ACD were accompanied by MrgprB2-associated changes in DRG neuronal excitability.

3.6.1 WSS Reduces DRG Neuronal Excitability in the C57BL/6J ACD Model but Not in MrgprB2$^{-/-}$ Mice

We measured the excitability of cervical DRG neurons across experimental groups in both mouse strains (Figure 9A, F). Excitability was assessed by the number of evoked action potentials. The number of action potentials was higher in both model groups than in the corresponding control groups. In C57BL/6J mice, WSS treatment significantly reduced the number of action potentials relative to the model group (Figure 9C), whereas no significant effect was observed in MrgprB2$^{-/-}$ mice (Figure 9H).

We next measured the rheobase of DRG neurons (Figure 9B,G). Rheobase was

significantly lower in both model groups than in the corresponding control groups, indicating increased neuronal excitability (Figure 9D,I). WSS did not significantly reverse the reduction in rheobase in either strain, although a nonsignificant trend toward recovery was observed in C57BL/6J mice (Figure 9D). In C57BL/6J mice, the resting membrane potential was significantly depolarized in the model group, and WSS attenuated this ACD-induced depolarization (Figure 9E). No significant change in resting membrane potential was detected in MrgprB2$^{-/-}$ mice (Figure 9J).

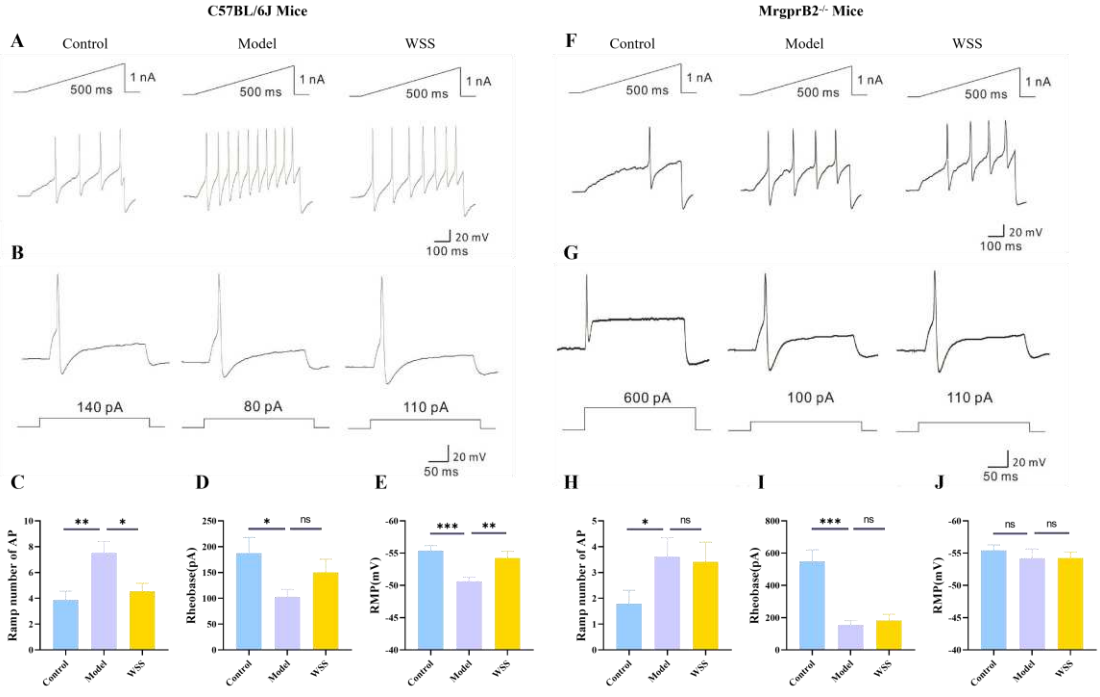

Figure 9. Effects of WSS on DRG neuronal excitability in ACD models of two mouse genotypes

(A) Action potentials evoked by ramp-current stimulation in DRG neurons from C57BL/6J mice (control: n = 26; model: n = 25; WSS: n = 24); (B) rheobase of DRG neurons from C57BL/6J mice; (C) number of evoked action potentials in DRG neurons from C57BL/6J mice; (D) rheobase of DRG neurons from C57BL/6J mice; (E) resting membrane potential of DRG neurons from C57BL/6J mice; (F) action

potentials evoked by ramp-current stimulation in DRG neurons from MrgprB2$^{-/-}$ mice (control: n = 20; model: n = 23; WSS: n = 23); (G) rheobase of DRG neurons from MrgprB2$^{-/-}$ mice; (H) number of evoked action potentials in DRG neurons from MrgprB2$^{-/-}$ mice; (I) rheobase of DRG neurons from MrgprB2$^{-/-}$ mice; (J) resting membrane potential of DRG neurons from MrgprB2$^{-/-}$ mice. Data are presented as the mean ± SEM. $^{*}p < 0.05$; $^{**}p < 0.01$; $^{***}p < 0.001$; ns, not significant.

3.6.2 WSS Does Not Alter Sodium Currents in DRG Neurons in Either ACD Model

Voltage-gated sodium currents were classified as TTX-R or TTX-S. We first recorded total sodium currents in cervical DRG neurons from each group in both mouse strains (Figure 10A,E). TTX-R currents were recorded after 3 min of TTX perfusion, and TTX-S currents were calculated by subtracting TTX-R currents from total sodium currents (Figure 10A, E).

Statistical analysis showed that WSS did not significantly alter the ACD-associated changes in total sodium currents in either mouse strain (Figure 10B, F). Further analysis showed that WSS did not significantly affect the ACD-associated changes in TTX-R sodium currents in either strain (Figure 10C, G). Likewise, WSS did not significantly affect the ACD-associated changes in TTX-S sodium currents in C57BL/6J or MrgprB2$^{-/-}$ mice (Figure 10D, H).

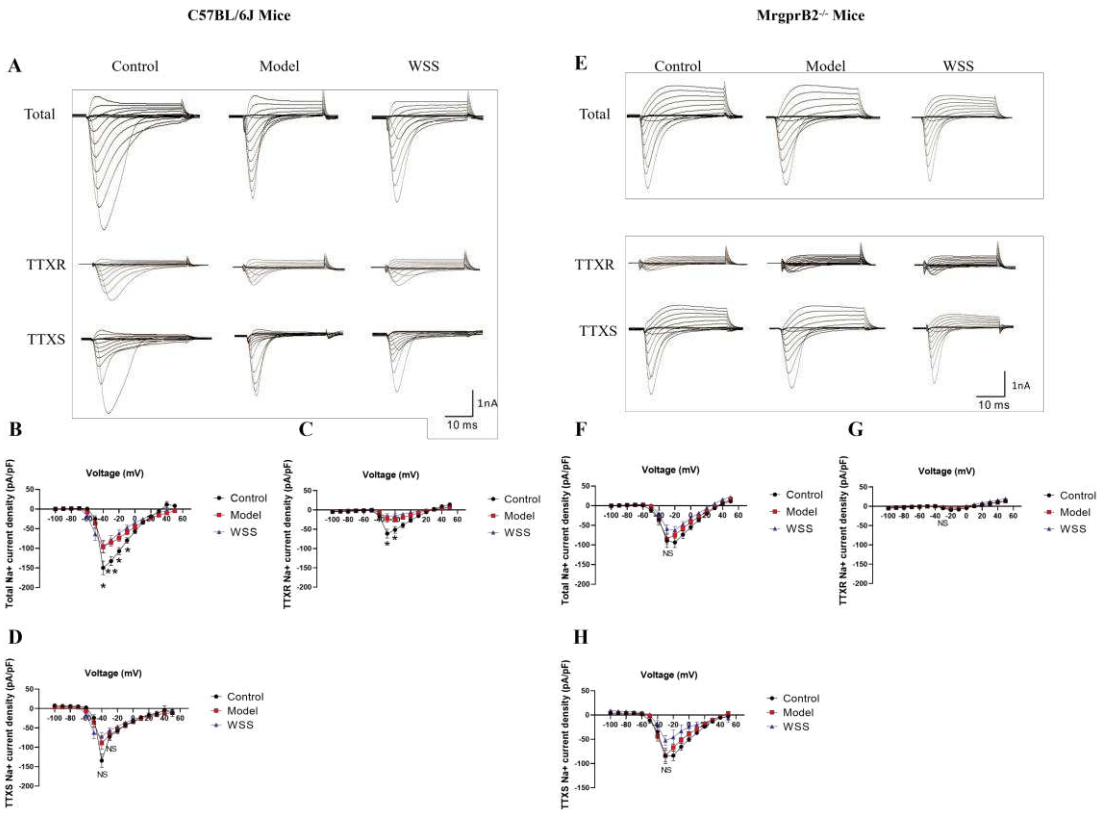

Figure 10. Effects of WSS on voltage-gated sodium currents in DRG neurons from two mouse ACD models

(A) Total voltage-gated sodium currents, TTX-R sodium currents, and TTX-S sodium currents in DRG neurons from C57BL/6J mice (control: n = 26; model: n = 15; WSS: n = 18); (B) changes in the amplitude of total sodium currents in DRG neurons from C57BL/6J mice; (C) changes in the amplitude of TTX-R sodium currents in DRG neurons from C57BL/6J mice; (D) changes in the amplitude of TTX-S sodium currents in DRG neurons from C57BL/6J mice; (E) total, TTX-R, and TTX-S sodium currents in DRG neurons from MrgprB2$^{-/-}$ mice (control: n = 21; model: n = 26; WSS: n = 19); (F) changes in the amplitude of total voltage-gated sodium currents in DRG neurons from MrgprB2$^{-/-}$ mice; (G) changes in the amplitude of TTX-R sodium currents in DRG neurons from MrgprB2$^{-/-}$ mice; (H) changes in the amplitude of

509 TTX-S sodium currents in DRG neurons from MrgprB2$^{-/-}$ mice. Data are presented as
510 the mean ± SEM. $^{*}p < 0.05$; $^{**}p < 0.01$; ns, not significant.
511
512 3.6.3 WSS Attenuates the Reduction in Sustained Potassium Currents in DRG
513 Neurons in an MrgprB2-Associated Manner
514 Total potassium currents were recorded in cervical DRG neurons from each
515 group in both mouse strains (Figure 11A, E). Sustained potassium currents were then
516 recorded, and transient potassium currents were calculated by subtracting sustained
517 currents from total currents (Figure 11A, E).
518 In C57BL/6J mice, total potassium currents were significantly lower in the
519 model group than in the control group, and WSS significantly attenuated this
520 ACD-associated reduction (Figure 11B). In MrgprB2$^{-/-}$ mice, total potassium currents
521 did not differ significantly among groups (Figure 11F). Sustained potassium currents
522 were also significantly lower in the C57BL/6J model group, and WSS significantly
523 attenuated this reduction (Figure 11C); no significant group differences were observed
524 in MrgprB2$^{-/-}$ mice (Figure 11G). Transient potassium currents did not differ
525 significantly among groups in either strain (Figure 11D,H). These findings suggest
526 that WSS may attenuate ACD-associated membrane-potential depolarization by
527 preserving sustained potassium currents in DRG neurons; the absence of this effect in
528 MrgprB2$^{-/-}$ mice implicates MrgprB2 in the response.

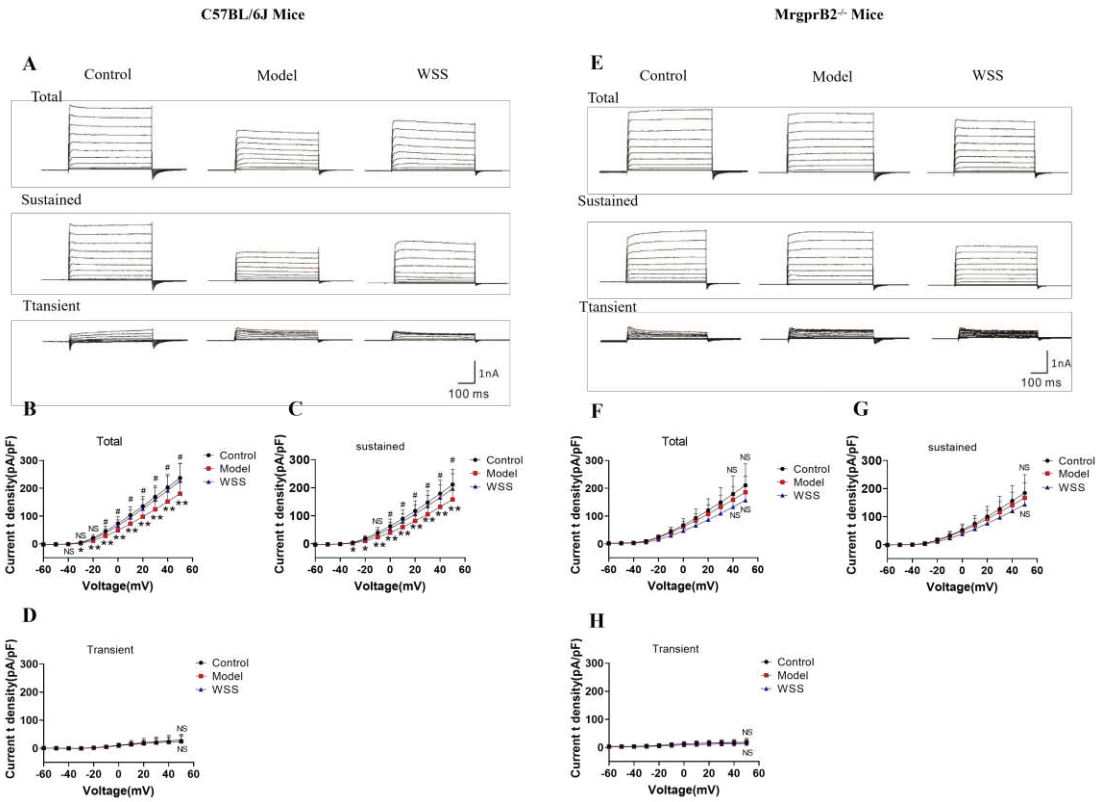

Figure 11. Effects of WSS on voltage-gated potassium currents in DRG neurons from two mouse ACD models

(A) Total voltage-gated potassium currents, sustained potassium currents, and transient potassium currents in DRG neurons from C57BL/6J mice (control: n = 22; model: n = 16; WSS: n = 24); (B) changes in the amplitude of total potassium currents in DRG neurons from C57BL/6J mice; (C) changes in the amplitude of sustained potassium currents in DRG neurons from C57BL/6J mice; (D) changes in the amplitude of transient potassium currents in DRG neurons from C57BL/6J mice; (E) total, sustained, and transient potassium currents in DRG neurons from MrgprB2$^{-/-}$ mice (control: n = 28; model: n = 24; WSS: n = 19); (F) changes in the amplitude of total voltage-gated potassium currents in DRG neurons from MrgprB2$^{-/-}$ mice; (G) changes in the amplitude of sustained potassium currents in DRG neurons from

MrgprB2$^{-/-}$ mice; (H) changes in the amplitude of transient potassium currents in DRG neurons from MrgprB2$^{-/-}$ mice. Data are presented as the mean ± SEM. $^{*}p < 0.05$; $^{**}p < 0.01$; ns, not significant.

4. Discussion

Using C57BL/6J and MrgprB2$^{-/-}$ mice and integrating gut microbiome profiling, serum metabolomics, and whole-cell patch-clamp electrophysiology, this study showed that WSS ameliorated ACD-associated skin lesions and pruritus and restored sustained potassium currents in DRG neurons. These effects were observed in C57BL/6J mice but were absent or attenuated in MrgprB2$^{-/-}$ mice, implicating MrgprB2 in the response to WSS.

MrgprB2 is predominantly expressed in connective-tissue mast cells and is an important mediator of allergic pruritus and pseudoallergic reactions [16]. Hapten exposure in contact dermatitis may directly or indirectly activate MrgprB2 on mast cells, inducing degranulation and release of mediators such as histamine, 5-HT, and TNF-α. These mediators can sensitize DRG neurons and promote pruritic and inflammatory responses [17].

Skin-lesion scores and scratching behavior showed that WSS ameliorated ACD lesions and pruritus in C57BL/6J mice, with effects comparable to those of hydrocortisone. In MrgprB2$^{-/-}$ mice, WSS did not significantly improve either outcome, whereas hydrocortisone remained effective. These findings implicate MrgprB2 in the therapeutic response to WSS and suggest that the mechanism of WSS

differs from the broad anti-inflammatory effects of glucocorticoids.

The gut microbiota can influence cutaneous immune homeostasis through the "gut-skin axis," and both compositional and functional dysbiosis have been associated with inflammatory skin diseases, including atopic dermatitis and contact dermatitis [18]. WSS did not significantly alter the alpha diversity of the gut microbiota but markedly changed overall community structure in C57BL/6J ACD mice. This structural remodeling was attenuated in MrgprB2$^{-/-}$ mice, suggesting that the microbial response to WSS may be partly associated with MrgprB2 signaling. At the genus level, WSS restored the reduced relative abundance of *Ligilactobacillus* and increased the relative abundance of Odoribacter in ACD mice. *Ligilactobacillus* is considered a beneficial gut genus, and studies indicate that its members may alleviate allergic skin inflammation by strengthening the intestinal mechanical barrier, modulating the Th1/Th2 immune balance, and reducing the release of pro-inflammatory mediators [19]. *Odoribacter* is an important producer of SCFAs. Its metabolites, including butyrate and propionate, can exert systemic anti-inflammatory effects [20,21] and may enter the circulation and influence ion-channel function and neuronal excitability in peripheral sensory neurons [22].

PICRUSt2 predicted increased abundances of pathways related to glycine, serine, and threonine metabolism; alanine, aspartate, and glutamate metabolism; amino acid biosynthesis; and carbon metabolism after WSS treatment. Products associated with these pathways, including glycine, glutamate, and serine, are neuroactive amino acids that can act on receptors or ion channels in DRG neurons and thereby modulate

586 excitability [23,24]. These findings suggest that WSS may restore beneficial taxa and
587 alter microbial amino acid and energy metabolism. Such changes could contribute to
588 improved systemic immune homeostasis and, through circulating microbial
589 metabolites, indirectly influence DRG neuronal function and ACD-associated
590 pruritus.

591 The serum metabolome provides a functional bridge between the gut microbiota
592 and host phenotype and can directly reflect the functional state of the organism. WSS
593 partially reversed serum metabolic abnormalities in ACD mice. Moreover, the
594 enriched pathways associated with WSS showed little overlap between C57BL/6J and
595 MrgprB2$^{-/-}$ mice, further indicating genotype-dependent metabolic responses. In
596 C57BL/6J mice, differential metabolites were mainly enriched in three pathways:
597 mineral absorption, ABC transporters, and FcγR-mediated phagocytosis. Mineral
598 absorption contributes to the homeostasis of potassium, sodium, calcium, and other
599 cations. Transmembrane gradients of these ions underlie neuronal resting potentials
600 and action-potential firing [25]. Thus, WSS-associated enrichment of this pathway
601 may indicate restoration of the ionic microenvironment required for normal electrical
602 activity in DRG neurons. ABC transporters are widely expressed in immune cells and
603 neurons and participate in the transmembrane transport of inflammatory mediators,
604 lipids, and ions. Their dysfunction has been linked to the progression of cutaneous
605 inflammation and neuronal sensitization [26]. FcγR-mediated phagocytosis
606 contributes to the clearance of immune complexes and the initiation of inflammation
607 resolution [27]. Enrichment of this pathway may therefore reflect enhanced

608 inflammatory clearance and tissue repair. In MrgprB2$^{-/-}$ mice, WSS-associated
609 metabolites were instead enriched in nucleotide and pyrimidine metabolism and folate
610 biosynthesis. The lack of overlap between genotypes suggests that MrgprB2 deletion
611 substantially altered the direction of the metabolic response to WSS.

612 ELISA findings were consistent with the phenotypic results. In C57BL/6J ACD
613 mice, cutaneous TNF-α, IL-4, 5-HT, and CXCL10 levels were elevated and were
614 significantly reduced after WSS treatment. In MrgprB2$^{-/-}$ mice, WSS produced
615 smaller changes in 5-HT and IL-4 and did not significantly alter TNF-α or CXCL10.
616 Because MrgprB2 activation is an upstream trigger of mast-cell degranulation [5],
617 these findings are consistent with the possibility that WSS reduces mast-cell
618 activation and thereby lowers local concentrations of inflammatory and pruritogenic
619 mediators [28-31]. However, direct inhibition of MrgprB2 was not measured. The
620 residual effects in MrgprB2$^{-/-}$ mice may reflect MrgprB2-independent systemic
621 immunomodulation, potentially involving the gut microbiota.

622 DRG neuronal hyperexcitability is a key electrophysiological basis of peripheral
623 sensitization in pruritus, and altered ion-channel function can directly modify
624 neuronal excitability [32]. In the present study, ACD was associated with increased
625 action-potential firing, reduced rheobase, and depolarized resting membrane potential
626 in DRG neurons. These changes are consistent with the characteristic features of
627 peripheral sensory-neuron sensitization. WSS attenuated several of these excitability
628 changes in C57BL/6J mice but not in MrgprB2$^{-/-}$ mice. Isolation and analysis of
629 specific ion-current classes further showed that WSS restored sustained voltage-gated

potassium currents but did not significantly alter total, TTX-S, or TTX-R sodium currents. Sustained potassium currents help maintain the neuronal resting membrane potential and regulate action-potential repolarization. Suppression of these currents can depolarize the membrane and increase neuronal excitability, contributing to peripheral sensitization in chronic pruritus and pain [33]. MrgprB2 is a Gq-coupled receptor whose activation can engage downstream PKC and PLC-IP3 signaling [6], and these pathways can modulate ion-channel activity. On the basis of the present findings, we propose that WSS preserves sustained potassium-current amplitude, reverses membrane-potential depolarization and neuronal sensitization, and thereby alleviates pruritus. However, the specific link between MrgprB2 signaling and potassium-channel regulation in DRG neurons remains to be established. Direct receptor antagonism by WSS, neuronal MrgprB2 expression, and downstream channel phosphorylation were not measured and require experimental confirmation.

Notably, total sodium currents in DRG neurons were lower in the ACD model, contrary to the conventional expectation that increased excitability would be accompanied by increased sodium currents; this pattern occurred in both genotypes [34]. One possible explanation is the timing of measurement. Recordings were obtained on day 3 after model induction, during the transition from acute to subacute inflammation. At this stage, compensatory sodium-channel downregulation may limit neuronal overexcitation [35]. Alternatively, complex regulation by inflammatory mediators may produce different temporal changes in individual sodium-channel subtypes, including Nav1.7, Nav1.8, and Nav1.9. Total sodium current would

therefore not fully reflect subtype-specific functional changes [36]. Subtype-specific recordings across multiple time points will be needed to determine the mechanism underlying this observation.

This study has several limitations. First, microbial functions were inferred from 16S rRNA gene sequencing using PICRUSt2 and were not validated by metagenomic sequencing or targeted metabolomics. The causal relationships among the gut microbiota, circulating metabolites, and neuronal function therefore remain unresolved. Second, WSS is a complex aqueous herbal extract containing flavonoids, alkaloids, organic acids, and other constituents. The component or components that interact with MrgprB2 have not been identified. Bioactivity-guided fractionation, receptor-binding studies, and target-engagement assays are needed. Third, a direct causal link between the gut microbiota and DRG excitability was not tested. Fecal microbiota transplantation, antibiotic-depletion or germ-free models, and metabolite-rescue experiments could clarify the proposed "microbiota-metabolism-nerve" axis.

5. Conclusion

By integrating microbiome and metabolome profiling with whole-animal, tissue, molecular, and electrophysiological analyses, this study showed that WSS ameliorated ACD-associated lesions and pruritus and restored sustained potassium currents in DRG neurons in C57BL/6J mice. The attenuation or loss of these effects in MrgprB2$^{-/-}$ mice implicates MrgprB2 in the response to WSS. Further studies are

required to identify the active constituents, demonstrate direct target engagement, and establish causal links among the gut microbiota, host metabolism, and neuronal excitability.

List of abbreviations

ACD: Allergic contact dermatitis

DRG: Dorsal root ganglia

MrgprB2: Mas-related G protein-coupled receptor B2

S. Scandens: *Senecio scandens* Buch.-Ham. ex D. Don

WSS: Water extract of *S. scandens*

SPF: Specific pathogen-free

IL-17A: Interleukin-17A

IL-1β: Interleukin-1β

TNF-α: Tumor Necrosis Factor α

IL-4: Interleukin-4

IL-13:Interleukin-13

HIS: Histamine

5-HT: 5-hydroxytryptamine

CXCL10: C-X-C motif chemokine ligand 10

TPSβ2: Trypsin Beta 2

HC: Hydrocortisone

UHPLC: Ultra-high performance liquid chromatography

QC: Quality control

ESI: Electrospray ionization

m/z: Mass-to-charge ratio

PCA: Principal component analysis

OPLS-DA: Orthogonal partial least squares-discriminant analysis

VIP:Variable importance in the projection

KEGG: Kyoto Encyclopedia of Genes and Genomes

TTX: Tetrodotoxin

TTX-R: TTX-resistant

TTX-S: TTX-sensitive

One-Way ANOVA: One-way analysis of variance

SEM: Standard error of the mean

TICs: Total ion chromatograms

PCoA: Principal coordinate analysis

SCFAs: Short-chain fatty acids

Ethics approval and consent to participate

The animal experiments were approved by the Jishou University Biomedical Ethics Committee (No. JSDX-2025-0080).

Consent for publication

All authors confirm their consent for publication the manuscript.

Availability of data and materials

The datasets used and/or analysed during the current study are available from the corresponding author on reasonable request.

Competing interests

The authors declare that they have no competing interests.

Funding

This study was funded by the Hunan Provincial Natural Science Foundation of China (No. 2026JJ80705) and the Hunan Provincial Graduate Scientific Research Innovation Program (No. LXBZZ2024302).

Authors' contributions

JS: Writing-original draft, Methodology, Investigation, Validation, Formal analysis, Funding acquisition. JZ: Investigation, Validation, Formal analysis. BL: Investigation, Resources, Methodology. QC: Investigation, Methodology, Resources. FY: Methodology, Investigation, Validation, Supervision, Project administration, Funding acquisition, Writing-review & editing. GC: Supervision, Project administration, Writing-review & editing. All authors reviewed the manuscript.

Acknowledgements

We sincerely appreciate the anonymous reviewers for their valuable, perceptive comments.

References

1. Sung CT, McGowan MA, Machler BC, Jacob SE. Systemic treatments for allergic contact dermatitis. Dermatitis. 2019;30(1):46-53.
2. Nicolet E, Bobeica C, Tatu AL. Glucocorticoid-induced skin atrophy: the old and the new. Clin Cosmet Investig Dermatol. 2020;13:1041-1050.
3. Singto T, Sergeeva A, Filor V, Vidak J, Kleuser B, Belik V, et al. Immune cells in dorsal root ganglia are associated with pruritus in a mouse model of allergic contact dermatitis and co-culture study. J Neuroimmunol. 2025;404:578617.
4. Voisin T, Chiu IM. Mast cells get on your nerves in itch. Immunity. 2019;50(5):1117-1119.
5. McNeil B, Pundir P, Meeker S, Han L, Undem B, Kulka M, et al. Identification of a mast-cell-specific receptor crucial for pseudo-allergic drug reactions. Nature. 2015;519:237-241.
6. Ye F, Jiang Y, Zong Y, Zhang J, Zhu C, Yang Y, et al. PLC-IP3-ORAI pathway participates in the activation of the MRGPRB2 receptor in mouse peritoneal mast cells. Immunol Lett. 2022;248:37-44.
7. Green DP, Limjunyawong N, Gour N, Pundir P, Dong X. A mast-cell-specific receptor mediates neurogenic inflammation and pain. Neuron. 2019;101(3):412-420.
8. Meng F, Zhang X, Xie W. Research progress of the herbs of Senecio scandens. J Northeast Agric Univ. 2010;41(9):156-160.
9. Ye F, Jiang Y, Zhang J, Zong Y, Yu M, Chen C, et al. Water extract of Senecio

762 scandens Buch.-Ham ameliorates pruritus by inhibiting MrgprB2 receptor. J
763 Inflamm Res. 2022;15:5989-5998.
764 10. Lomax AE, Pradhananga S, Sessenwein JL, O'Malley D. Bacterial modulation of
765 visceral sensation: mediators and mechanisms. Am J Physiol Gastrointest Liver
766 Physiol. 2019;317(3):G363-G372.
767 11. Luo D, Deng T, Yuan W, Deng H, Jin M. Plasma metabolomic study in Chinese
768 patients with wet age-related macular degeneration. BMC Ophthalmol.
769 2017;17(1):165.
770 12. Gu Z, Li L, Tang S, Liu C, Fu X, Shi Z, et al. Metabolomics reveals that
771 crossbred dairy buffaloes are more thermotolerant than Holstein cows under
772 chronic heat stress. J Agric Food Chem. 2018;66(49):12889-12897.
773 13. Sun X, He L, Liu H, Thorne RF, Zeng T, Liu L, et al. The diapause-like
774 colorectal cancer cells induced by SMC4 attenuation are characterized by low
775 proliferation and chemotherapy insensitivity. Cell Metab. 2023;35(9):1563-1579.
776 14. Ma JH, Xu B, Liu B, Zhang CH, Zhang XP, Chai Q, et al. Mechanism of
777 antibiotics aggravating allergic rhinitis in mice based on untargeted metabolomics.
778 Chin Pharmacol Bull. 2025;41(2):1-9.
779 15. Prins FM, Collij V, Groot HE, Björk JR, Swarte JC, Andreu-Sánchez S, et al. The
780 gut microbiome across the cardiovascular risk spectrum. Eur J Prev Cardiol.
781 2024;31(8):935-944.
782 16. Thapaliya M, Chompunud Na Ayudhya C, Amponnawarat A, Roy S, Ali H. Mast
783 cell-specific MRGPRX2: a key modulator of neuro-immune interaction in

allergic diseases. Curr Allergy Asthma Rep. 2021;21(1):3.

17. Meixiong J, Anderson M, Limjunyawong N, Sabbagh MF, Hu E, Mack MR, et al. Activation of mast-cell-expressed mas-related G-protein-coupled receptors drives non-histaminergic itch. Immunity. 2019;50(5):1163-1171.

18. Guevara-Ramírez P, Paz-Cruz E, Ruiz-Pozo VA, Cadena-Ullauri S, Tamayo-Trujillo R, Cadena A, et al. Atopic dermatitis beyond cutaneous inflammation: the interplay between progesterone, testosterone, gut microbiota, and immune dysregulation. Microorganisms. 2026;14(7):1565.

19. Chuandong Z, Hu J, Li J, Wu Y, Wu C, Lai G, et al. Distribution and roles of Ligilactobacillus murinus in hosts. Microbiol Res. 2024;282:127648.

20. Guo C, Wang Y, Zhang S, Zhang X, Du Z, Li M, et al. Crataegus pinnatifida polysaccharide alleviates colitis via modulation of gut microbiota and SCFAs metabolism. Int J Biol Macromol. 2021;181:357-368.

21. Gomez-Arango LF, Barrett HL, McIntyre HD, Callaway LK, Morrison M, Dekker Nitert M. Increased systolic and diastolic blood pressure is associated with altered gut microbiota composition and butyrate production in early pregnancy. Hypertension. 2016;68(4):974-981.

22. Senarath R, Oikari LE, Bharadwaj P, Jayasena V, Martins RN, Fernando W. Butyrate and lauric acid effect on astrocytes and neurons in Alzheimer's disease. Alzheimers Dement. 2024;20:e092277.

23. Yao L, Zhang TY, Diao XT, Ma JJ, Bai HH, Suo ZW, et al. Functional expression of glycine receptors in DRG neurons of mice. Eur J Pharmacol.

2021;899:174034.

24. Malet M, Brumovsky PR. VGLUTs and glutamate synthesis—focus on DRG neurons and pain. Biomolecules. 2015;5(4):3416-3437.

25. Petratou D, Gjikolaj M, Kaulich E, Schafer W, Tavernarakis N. A proton-inhibited DEG/ENaC ion channel maintains neuronal ionstasis and promotes neuronal survival under stress. iScience. 2023;26(7).

26. Grube M, Hagen P, Jedlitschky G. Neurosteroid transport in the brain: role of ABC and SLC transporters. Front Pharmacol. 2018;9:354.

27. Loike JD, Shabtai DY, Neuhut R, Malitzky S, Lu E, Husemann J, et al. Statin inhibition of Fc receptor–mediated phagocytosis by macrophages is modulated by cell activation and cholesterol. Arterioscler Thromb Vasc Biol. 2004;24(11):2051-2056.

28. Leung L, Cahill CM. TNF-α and neuropathic pain - a review. J Neuroinflammation. 2010;7:27.

29. Seegraber M, Srour J, Walter A, Knop M, Wollenberg A. Dupilumab for treatment of atopic dermatitis. Expert Rev Clin Pharmacol. 2018;11(5):467-474.

30. Yoshimura M, Hachisuka J, Furue M. In vivo analysis of 5-HT-inudced pruritic response in rat DRG C neurons. Neurosci Res. 2010;68:e50.

31. Qu L, Fu K, Shimada SG, LaMotte R. Cl- channel is required for CXCL10-induced neuronal activation and itch response in a murine model of allergic contact dermatitis. J Neurophysiol. 2017;118(1):619-624.

32. Cho H, Chung S, Shim WS, Lee B, Kim H, Oh U, et al. Anoctamin 1/TMEM16A

in pruritoceptors is essential for Mas-related G protein receptor–dependent itch. Pain. 2022;163(11):2172-2184.

33. Biet M, Dansereau MA, Sarret P, Dumaine R. The neuronal potassium current IA is a potential target for pain during chronic inflammation. Physiol Rep. 2021;9(16):e14975.

34. Jang K, Garraway S. A review of dorsal root ganglia and primary sensory neuron plasticity mediating inflammatory and chronic neuropathic pain. Neurobiol Pain. 2024;15:100151.

35. Cui A, Meng X, Wang Z, Wu Q, Li M. Dorsal root ganglion as a hub for peripheral sensitization: a hierarchical regulation model and translational progress. J Pain Res. 2026;19:601365.

36. Xie Y, Huang X, Lu F, Huang J. Targeting Nav channels for pain relief: structural insights and therapeutic opportunities. Int J Mol Sci. 2026;27(3):1180.

Supplementary Files

This is a list of supplementary files associated with this preprint. Click to download.

- SupplementaryMaterials.docx